ELSEVIER

Chemical Engineering Journal 83 (2001) 107–121

Chemical Engineering Journal

www.elsevier.com/locate/cej

On the isothermal binary mass transport in a single pore

Piet J.A.M. Kerkhof*, Marcel A.M. Geboers, Krzysztof J. Ptasinski

Department of Chemical Engineering and Chemistry, Eindhoven University of Technology, PO Box 513, 5600 MB Eindhoven, Netherlands

Received 4 January 2000; received in revised form 17 July 2000; accepted 19 July 2000

Abstract

For the transport in an inert pore the local species momentum balance is reconsidered. This leads to a Maxwell–Stefan type equation for a component α in which the gradient in chemical potential, the interspecies friction and the α–α shear stress form the momentum balance. From the set of equations the component axial velocity profiles can be derived, and so we call this model the velocity profile model (VPM-1), in which 1 stands for the fact that we only consider here the flow in one direction. For binary systems the set of equations is solved, and pore-integrated velocities are derived. This is done both for liquids with a no-slip boundary condition and for gases with Maxwell-slip boundary condition. The pore-averaged velocities can be expressed in the same form as the binary friction model. The use of the difference in pore-averaged velocities instead of the pore-averaged differences requires a correction function, which is derived for both fluid types. For liquids the component-wall friction factors are equal to those in the binary friction model, for gases a slightly different form is obtained. Comparison of predictions for liquid ultrafiltration and gas transport through porous plugs shows in general very small differences between the present model and the BFM, and good agreement with experimental data. The VPM-1 predicts a second flow reversal point of (near-)equal mass isobaric diffusion of gases at different pressures, and a reversal with temperature. From the model follows a new expression for the velocity difference. Velocity profiles for various situations are explored such as liquid ultrafiltration and diffusion, counterdiffusion of gases and for the Stefan-tube. In the latter we find that for a zero average flux of inert gas there is a core of inert gas moving in the direction of the water vapor, and a reverse flow in the area near the wall. The model can be extended to more-dimensional flow problems such as in adsorption and heterogeneous catalysis.

Keywords: Multicomponent diffusion; Dusty gas model; Maxwell–Stefan; Binary friction model; Baroeffect; Porous media

1. Introduction

The transport of mixtures in pores is of great interest for the modeling of a variety of separation processes, such as ultrafiltration, adsorption and drying, and for the transport in reaction systems such as heterogeneous catalysts and porous membrane reactors. Over the last 5 years the Science Citation Index shows 42 references to the "dusty gas model" of Mason et al. [1,2] and for a number of these papers there is an underlying Ph.D. Thesis. This indicates that the interest in multicomponent transport in pores is very lively, and we have the impression that it is growing. We have recently proven that the dusty gas model is invalid because of errors in the derivation [3]. Starting from the Lightfoot friction equation [4], one of us developed the "binary friction model" [3], which was shown to be in good agreement with experimental data both in liquid ultrafiltration [3,5] and transport of gas mixtures in capillaries and in porous graphite [3]. In recent textbooks of Wijngaarden et al. [6] and Keil [7] support was given to the viewpoints on the dusty gas model and on the development of the binary friction model. The relevance of the meso- and macropore resistance was demonstrated by Silva and Rodrigues [8], who found that in adsorption of *n*-hexane on zeolite 5A pellets that these resistances were completely rate-controlling. In the BFM the friction coefficients between components and the wall are expressed in terms of the permeability and partial viscosity coefficients, which can be estimated from free-fluid mixture viscosity data. Also based on the BFM some classic problems were studied such as the Stefan-tube, Graham's law and the Bosanquet equation [9]. Still lacking at present was a theoretical underpinning of the theory from first principles. Whitaker [10–12] very clearly showed the neglect of considering the momentum balances and velocity profiles for instance in considering the Stefan-tube by chemical engineers, and derived a criterion from the momentum balance to indicate if and when the usual assumption of flat velocity profiles would be practically justified. In various treatments of counterdiffusion in capillaries, such as by Kramers and Kistemaker [13], Waldmann and Schmitt [14], Lang and Eger [15] and Lang [16], no clear indication of velocity pro-

* Corresponding author. Tel.: +31-40-247-2973; fax: +31-40-243-9303.
E-mail address: p.j.a.m.kerkhof@tue.nl (P.J.A.M. Kerkhof).

1385-8947/01/$ – see front matter
PII: S1385-8947(00)00241-2

Nomenclature

A	constant, see Eq. (23) ($N\,m^{-4}\,s$)
B	force on component(s) per unit volume ($N\,m^{-3}$)
B_0	pore permeability, see Eq. (28) (m^2)
c	molar concentration ($kmol\,m^{-3}$)
$\mathcal{Đ}$	Maxwell–Stefan diffusion coefficient ($m^2\,s^{-1}$)
D	diffusion coefficient ($m^2\,s^{-1}$)
d	constants, see Eq. (60)
F	function, see Eq. (13)
F	function, see Eq. (45)
f	function, see Eqs. (26a) and (26b)
f_r	coefficient of reflection (–)
$f_{\alpha m}$	friction coefficient for gases ($s\,m^{-2}$)
G	slip modulus (m)
g_D	ratio between averaged velocity difference and difference in averaged velocities (–)
h	function, see Eqs. (31) and (32)
I_0, I_1	modified Bessel functions of the first kind of order 0 and 1, respectively
K	constant, see Eq. (10) (–)
$K_{\alpha\beta}$	coefficients in slip flow equation (42)
k_B	Boltzmann constant (kJ per molecule K^{-1})
M	molecular mass ($kg\,kmol^{-1}$)
N	flux ($kmol\,m^{-2}\,s^{-1}$)
n	molecular density ($molecules\,m^{-3}$)
P	pressure (Pa)
$Q_{\alpha\beta}$	coefficient for averaged velocities, see Eqs. (46) and (47)
r	coordinate (m)
R	half distance between two infinite plates, capillary radius (m)
R_g	gas constant ($kJ\,kmol^{-1}\,K^{-1}$)
T	temperature (K)
u	velocity ($m\,s^{-1}$)
$\bar{V}$	specific molar volume ($m^3\,kmol^{-1}$)
x	coordinate (m)
x	mole fraction (–)
z	coordinate (m)
$<>$	pore-averaged

Greeks

α	constant, see Eq. (9) (–)
α_p, β_p	barodiffusion constants, see Section 4.3
β	modulus, see Eq. (14) (–)
$\beta_{\alpha m}$	friction coefficient between component α and wall ($s\,m^{-2}$)
γ	constant, see Eq. (12) (N)
δ_{ij}	Kronecker delta (–)
ε	element of stress tensor (s^{-1})
ζ_α, $\zeta_{\alpha\beta}$	ratio of Knudsen to molecular diffusion coefficients, see Eq. (44) (–)
η	(partial) viscosity (Pa s)
κ	fractional viscosity coefficient (s)
λ	root, see Eq. (29) (m^{-1})
Λ	mean free path (m)
μ	chemical potential ($kJ\,kmol^{-1}$)
ν	shape factor, see Eq. (25) (–)
ξ	dimensionless coordinate (–)
$\xi_{\alpha\beta}$	Wilke coefficient, see Eq. (56)
ϕ	volume fraction (–)
Φ	accounting factor for deviation between pore and free-fluid diffusion coefficient (–)
φ	modulus, see Eq. (27)
ω	weight fraction (–)

Subscripts

1, 2	component, coordinate
i, j, k, l	coordinate number
m	wall, membrane
s	slip
t	total
α	component
β	component

Superscripts

0	zero-pressure limit, pure-component
K	Knudsen
v	normal region
$\sim$	three-dimensional vector
∞	infinite pore size

files was taken into account. In detailed partial studies of the baroeffect the statistical mechanics treatments did not lead to expressions readily to be converted to average fluxes over the pore diameter, e.g. Lang and Loyalka [17]. The notable exception is the work of Zhdanov and Roldughin [18,19] on gas diffusion in capillaries which was also partially inaccessible due to incompleteness of mentioning the complete equations for the averaged and the diffusion velocities, as desirable for the chemical engineer. However, their work culminated in an overview paper in which expressions were given for the velocity difference of the species and the mass-averaged velocities in transport in a capillary [20], the latter for the Knudsen region. We will come back to this later. In their comments on the dusty gas model they also presented the species momentum balance for gas-phase diffusion at very small Knudsen numbers, as followed from statistical mechanics. In the absence of external forces this reads

$$\frac{\partial P_\alpha}{\partial x_i} - \eta_\alpha \frac{\partial \varepsilon_{ik}}{\partial x_k} = -\sum_\beta \frac{n_\alpha n_\beta k_B T}{n \mathcal{Đ}_{\alpha\beta}} (\tilde{u}_\alpha - \tilde{u}_\beta) = -P_t \sum_\beta \frac{x_\alpha x_\beta}{\mathcal{Đ}_{\alpha\beta}} (\tilde{u}_\alpha - \tilde{u}_\beta) \quad (1)$$

in which

$$\varepsilon_{ik} = \frac{\partial u_i}{\partial x_k} + \frac{\partial u_k}{\partial x_i} - \frac{2}{3}\delta_{ik}\frac{\partial u_l}{\partial x_l} \tag{2}$$

and the k and l subscripts indicate Einstein summation over the coordinate directions. The η_α are the partial viscosities, for which

$$\sum_\alpha \eta_\alpha = \eta_t \tag{3}$$

holds, with η_t the viscosity of the mixture.

They note that the viscous forces are not accounted for correctly in the DGM, and that also another "defect of the dusty gas model lies in the fact that it does not take into account the contributions of thin Knudsen layers into the fluxes at small Knudsen numbers" [20].

For the case of only axial velocity in the x-direction between two infinite plates, Eq. (1) goes over in

$$\frac{\partial P_\alpha}{\partial x} - \eta_\alpha \frac{\partial^2 u}{\partial z^2} = -P_t \sum_\beta \frac{x_\alpha x_\beta}{\mathcal{D}_{\alpha\beta}}(u_\alpha - u_\beta) \tag{4a}$$

or in a capillary:

$$\frac{\partial P_\alpha}{\partial x} - \eta_\alpha \frac{1}{r}\frac{\partial}{\partial r}\left(r\frac{\partial u}{\partial r}\right) = -P_t \sum_\beta \frac{x_\alpha x_\beta}{\mathcal{D}_{\alpha\beta}}(u_\alpha - u_\beta) \tag{4b}$$

In these equations u stands for the mass-averaged velocity. Physically the terms can be associated with the gradient in chemical potential, the viscous friction and the intermolecular friction, respectively.

Kronberg [21] proposed a modified version of Eq. (4b):

$$\frac{\partial P_\alpha}{\partial x} - \eta_\alpha \frac{1}{r}\frac{\partial}{\partial r}\left(r\frac{\partial u_\alpha}{\partial r}\right) = -P_t \sum_\beta \frac{x_\alpha x_\beta}{\mathcal{D}_{\alpha\beta}}(u_\alpha - u_\beta) \tag{5}$$

and so in the second term the gradient in the component velocity rather than that in the mass-averaged velocity appears. He solved the equations for a binary system assuming slip boundary conditions of the form

$$r = R, \qquad u_\alpha = -\Lambda_\alpha \frac{\partial u_\alpha}{\partial r} \tag{6}$$

in which Λ_α is the mean free path of the component in the mixture. He posed relations for Λ_α equivalent to

$$\Lambda_\alpha = \frac{2\eta_\alpha D_\alpha^K}{RP_t} \tag{7}$$

in which the D_α^K are the Knudsen diffusion coefficients.

Unfortunately he did not publish his results, and they are only partially available in the student graduation report by Schoorlemmer [22]. In terms of the cross-section averaged flux of component 1 in a binary system, his equation for the so-called viscous flow model (VFM) reads

$$\langle N_{1x}\rangle \frac{R_g T}{P_t} = -D_1^{VFM}\frac{\partial x_1}{\partial x} - x_1 K_1^{VFM}\frac{\partial P_t}{\partial x} \tag{8}$$

with

$$D_1^{VFM} = \alpha_1 \mathcal{D}_{12} \tag{9}$$

$$K_1^{VFM} = \frac{1}{\eta_t}\left(B_0 + \frac{\eta_1 D_1^K}{P_t} - \alpha_1 x_2 \frac{\gamma_1}{P_t}\right) \tag{10}$$

$$\alpha_1 = \frac{D_1^K + (\eta_1/\eta_t)\mathcal{D}_{12}[F(\beta) - 1]}{x_1 D_2^K + x_2 D_1^K + \mathcal{D}_{12}F(\beta)} \tag{11}$$

$$\gamma_1 = \eta_1 x_2(\mathcal{D}_{12} + D_1^K) - \eta_2 x_1(\mathcal{D}_{12} + D_2^K) \tag{12}$$

$$F(\beta) = \frac{\beta}{2}\frac{I_0(\beta)}{I_1(\beta)} \tag{13}$$

$$\beta = \left(\frac{8B_0\eta_t x_1 x_2}{\eta_1\eta_2\mathcal{D}_{12}}\right)^{1/2} \tag{14}$$

The parameter β was identified by him as an inverse Knudsen number of the order R/Λ, with Λ the average molecular mean free path.

2. The velocity gradient term

The basic difference between the Zhdanov and the Kronberg equations (4b) and (5), is the expression of the viscous friction in the gradient in the mass-averaged and the component velocity, respectively. It is therefore of interest to investigate this matter somewhat further.

In Fig. 1, we have illustrated the elements of the momentum balance for a component α, for the case that we have

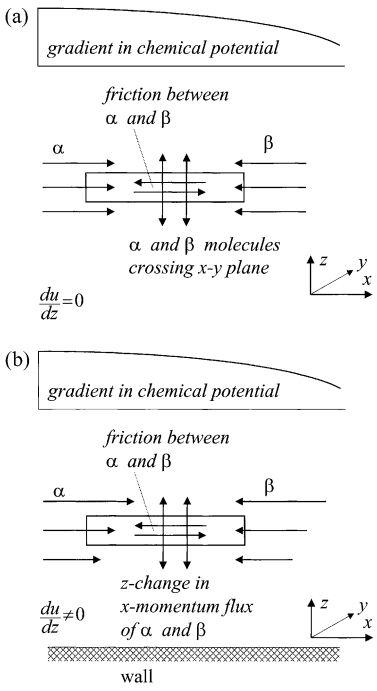

Fig. 1. Illustration of momentum balance on component α in a fluid: (a) without velocity gradients, and (b) with velocity gradients.

only axial velocities, in the x-direction, as well as gradients in the partial pressures in that direction only, and assuming the absence of external forces. Per unit volume there is a force on α because of the gradient in chemical potential. Let us first consider the situation without velocity gradients. For this situation we have the classical Maxwell–Stefan equation

$$\frac{\partial P_\alpha}{\partial x} = -P_t \sum_\beta \frac{x_\alpha x_\beta}{\mathcal{D}_{\alpha\beta}}(u_\alpha - u_\beta) \tag{15}$$

We have a change in x-momentum through the molecules of α and β passing through the x–z-planes, but also from molecules passing through the x–y planes. Since there are no velocity gradients, the α–α and β–β collisions will result in a zero momentum change. From the viewpoint of component α the momentum change will be thus the result of α–β collisions, caused by β-molecules entering through all planes of the volume element. Thus both lateral and axial α–β interactions are represented by the Maxwell–Stefan diffusion term, the r.h.s. of Eq. (15).

For a situation in which we have velocity gradients, still the α–β interaction caused by the flux of β-molecules through the x–y planes is accounted for in the diffusion term. Now, however, the α-molecules experience the momentum change due to collisions with the flux of α-molecules through the x–y planes with a velocity different from that in the volume element, and so we should add only the shear in terms of the velocity gradient of α, leading to the Kronberg type of equation.

Also we can see an inconsistency in the Zhdanov equation. For a simple situation like considered here, we can write for a binary system:

$$\begin{aligned}
\frac{\partial P_\alpha}{\partial x} - \eta_\alpha \frac{\partial^2 u}{\partial z^2} &= -P_t \frac{x_\alpha x_\beta}{\mathcal{D}_{\alpha\beta}}(u_\alpha - u_\beta),\\
\frac{\partial P_\beta}{\partial x} - \eta_\beta \frac{\partial^2 u}{\partial z^2} &= -P_t \frac{x_\alpha x_\beta}{\mathcal{D}_{\alpha\beta}}(u_\beta - u_\alpha)
\end{aligned} \tag{16}$$

For the mass-averaged velocity we have

$$u = \omega_\alpha u_\alpha + \omega_\beta u_\beta \tag{17}$$

Since we assumed no lateral concentration gradients, we may write

$$\frac{\partial^2 u}{\partial z^2} = \omega_\alpha \frac{\partial^2 u_\alpha}{\partial z^2} + \omega_\beta \frac{\partial^2 u_\beta}{\partial z^2} \tag{18}$$

Also we take the pressure constant over the z-direction, and so we obtain after addition of the equations for both components

$$\frac{\mathrm{d}P_t}{\mathrm{d}x} - \eta_t \frac{\partial^2 u}{\partial z^2} = 0 \tag{19}$$

which for the normal region, with no-slip boundary conditions gives

$$u = -\frac{1}{2\eta_t}(R^2 - z^2)\frac{\mathrm{d}P_t}{\mathrm{d}x}, \qquad \langle u\rangle = -\frac{R^2}{3\eta_t}\frac{\mathrm{d}P_t}{\mathrm{d}x} \tag{20}$$

This simple Poiseuille solution implies that under isobaric conditions the mass-averaged velocity would be zero, which is in conflict with experimental measurements. A similar argument can be made for liquid transport, and the result would be that no osmotic net flow could occur under isobaric circumstances. In the following we will further investigate the Kronberg type of equation.

3. Model development: the velocity profile model

The model to be developed here will be named the velocity profile model (VPM-1), to indicate that we consider here only one-dimensional flow without radial velocity and concentration profiles.

In order to generalize the model we consider the momentum balance on component α as formed by the gradient in chemical potential, by the shear friction due to α–α collisions and the α–β interactions characterized by the diffusion term.

We obtain the following equations for the two geometries:

$$\text{Infinite plates}: \quad B_\alpha - \eta_\alpha \frac{\partial^2 u_\alpha}{\partial z^2} = -P_t \sum_\beta \frac{x_\alpha x_\beta}{\mathcal{D}_{\alpha\beta}}(u_\alpha - u_\beta) \tag{21a}$$

$$\begin{aligned}
\text{Capillary}: \quad & B_\alpha - \eta_\alpha \frac{1}{r}\frac{\partial}{\partial r}\left(r\frac{\partial u_\alpha}{\mathcal{D}_{\partial r}}\right)\\
&= -P_t \sum_\beta \frac{x_\alpha x_\beta}{\mathcal{D}_{\alpha\beta}}(u_\alpha - u_\beta)
\end{aligned} \tag{21b}$$

with

$$B_\alpha = c_\alpha \left.\frac{\mathrm{d}\mu_\alpha}{\mathrm{d}x}\right|_T \tag{22}$$

3.1. Solution for two-component liquid phase transport

Here we have

$$\begin{aligned}
B_1 - \eta_1 \frac{\partial^2 u_1}{\partial z^2} &= -c_t R_g T \frac{x_1 x_2}{\mathcal{D}_{12}}(u_1 - u_2) = -A(u_1 - u_2),\\
B_2 - \eta_2 \frac{\partial^2 u_2}{\partial z^2} &= -A(u_2 - u_1), \quad A = c_t R_g T \frac{x_1 x_2}{\mathcal{D}_{12}}
\end{aligned} \tag{23}$$

for the infinite plates, and

$$\begin{aligned}
B_1 - \eta_1 \frac{1}{r}\frac{\partial}{\partial r}\left(r\frac{\partial u_1}{\partial r}\right) &= -A(u_1 - u_2)\\
B_2 - \eta_2 \frac{1}{r}\frac{\partial}{\partial r}\left(r\frac{\partial u_2}{\partial r}\right) &= -A(u_2 - u_1)
\end{aligned} \tag{24}$$

for the capillary.

We assume a symmetry condition at $z = 0$ or $r = 0$, respectively, and zero velocities at the wall, $u_\alpha(R) = 0$.

For the solution we find:

$$u_1 = -B_1\frac{B_0}{\eta_1}\varphi f(\lambda\xi) + \frac{\mathrm{d}P_\mathrm{t}}{\mathrm{d}x}\frac{B_0}{\eta_\mathrm{t}}\left[\varphi f(\lambda\xi) - \frac{\nu+2}{\nu}(1-\xi^2)\right]$$
$$u_2 = -B_2\frac{B_0}{\eta_2}\varphi f(\lambda\xi) + \frac{\mathrm{d}P_\mathrm{t}}{\mathrm{d}x}\frac{B_0}{\eta_\mathrm{t}}\left[\varphi f(\lambda\xi) - \frac{\nu+2}{\nu}(1-\xi^2)\right] \quad (25)$$

with ν a shape factor, which is 1 for the infinite plates, and 2 for the capillary, and $\xi = z/R$ and $\xi = r/R$, respectively.

$$\text{Infinite plates}: \quad f(\lambda\xi) = 1 - \frac{\cosh(\lambda R\xi)}{\cosh(\lambda R)} \quad (26a)$$

$$\text{Capillary}: \quad f(\lambda\xi) = 1 - \frac{I_0(\lambda R\xi)}{I_0(\lambda R)} \quad (26b)$$

Here we have defined a modulus:

$$\varphi = \frac{\mathcal{D}_{12}}{c_\mathrm{t}RTx_1x_2}\frac{\eta_1\eta_2}{\eta_\mathrm{t}B_0} \quad (27)$$

with B_0 the permeability,

$$B_0 = \frac{R^2}{(\nu+1)^2 - 1} \quad (28)$$

and the root λR is,

$$\lambda R = \sqrt{\frac{1}{\varphi}[(\nu+1)^2 - 1]} \quad (29)$$

The modulus φ may be regarded as a measure for the ratio between shear and diffusive friction, and is a modified form of that defined by Kronberg.

By integration over the cross-section we find the pore-averaged velocities:

$$\langle u_1\rangle = -B_1\frac{B_0}{\eta_1}\varphi h(\lambda R) - \frac{\mathrm{d}P_\mathrm{t}}{\mathrm{d}x}\frac{B_0}{\eta_\mathrm{t}}[1-\varphi h(\lambda R)],$$
$$\langle u_2\rangle = -B_2\frac{B_0}{\eta_2}\varphi h(\lambda R) - \frac{\mathrm{d}P_\mathrm{t}}{\mathrm{d}x}\frac{B_0}{\eta_\mathrm{t}}[1-\varphi h(\lambda R)] \quad (30)$$

with

$$\text{Infinite plates}: \quad h = 1 - \frac{1}{\lambda R}\tanh(\lambda R) \quad (31)$$

$$\text{Capillary}: \quad h = 1 - \frac{2}{\lambda R}\frac{I_1(\lambda R)}{I_0(\lambda R)} \quad (32)$$

In Fig. 2 the functions f and h are presented. For clarity we write out the chemical potential gradients:

$$B_\alpha = c_\alpha\left.\frac{\mathrm{d}\mu_\alpha}{\mathrm{d}x}\right|_T = c_\alpha\left.\frac{\mathrm{d}\mu_\alpha}{\mathrm{d}x}\right|_{P,T} + c_\alpha\bar{V}_\alpha\frac{\mathrm{d}P_\mathrm{t}}{\mathrm{d}x},$$
$$B_\mathrm{t} = \sum_\alpha B_\alpha = \frac{\mathrm{d}P_\mathrm{t}}{\mathrm{d}x} \quad (33)$$

The relative importance of the two terms on the r.h.s. of Eqs. (25) and (30) is determined on one hand by the ratio of the individual species driving force to the total driving force (pressure gradient) and on the other hand by the values of $\varphi f(\lambda\xi)$ and $\varphi h(\lambda R)$, respectively. Inspection of the functions $\varphi f(\lambda\xi)$ and $\varphi h(\lambda R)$ shows that for low values of φ, and so for dominant interspecies friction, these functions tend to go to zero, leading for both components to the same Poiseuille velocity profile in the non-isobaric case. For high values of φ, however, the limits of these functions are such that the second term on the r.h.s. of Eqs. (25) and (30) vanishes, and so we encounter another limit situation in which the transport of each component is only dependent on its individual driving force and its partial viscosity. We may call this limit "individual flow"; this occurs when the intraspecies friction is the dominating phenomenon. It is interesting to observe that the interspecies or "diffusive" friction tends to make the individual velocity profiles more coherent, while the intraspecies "viscous" friction tends to make them more diverging. As will be explored further on, in many practical situations both friction terms should be accounted for.

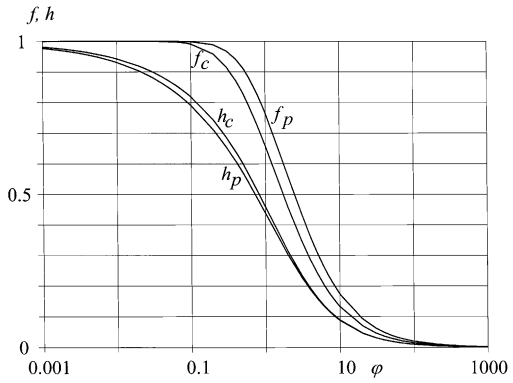

Fig. 2. Graphical representation of the functions f and h for infinite plates and cylindrical capillaries, as defined in Eqs. (26), (31) and (32), in dependence on the modulus φ, defined in Eq. (27).

3.2. Solution for two-component gas-phase transport

In gas-phase transport, we specify formally that at the walls we have a given slip velocity of the components:

$$z, r = R, \qquad u_\alpha = u_{\mathrm{s},\alpha} \quad (34)$$

and we obtain the solution as:

$$u_1 = u_{\mathrm{s},1} - \frac{\eta_2}{\eta_\mathrm{t}}(u_{\mathrm{s},1} - u_{\mathrm{s},2})f(\lambda\xi) + \frac{-B_1\eta_2\eta_\mathrm{t} + B_\mathrm{t}\eta_1\eta_2}{A\eta_\mathrm{t}^2}f(\lambda\xi) - \frac{R^2}{2\nu}\frac{B_\mathrm{t}}{\eta_\mathrm{t}}(1-\xi^2)$$
$$u_2 = u_{\mathrm{s},2} - \frac{\eta_1}{\eta_\mathrm{t}}(u_{\mathrm{s},2} - u_{\mathrm{s},1})f(\lambda\xi) + \frac{-B_2\eta_1\eta_\mathrm{t} + B_\mathrm{t}\eta_1\eta_2}{A\eta_\mathrm{t}^2}f(\lambda\xi) - \frac{R^2}{2\nu}\frac{B_\mathrm{t}}{\eta_\mathrm{t}}(1-\xi^2) \quad (35)$$

and for the pore-averaged velocities:

$$\langle u_1\rangle = u_{s,1} - \frac{\eta_2}{\eta_t}(u_{s,1}-u_{s,2})h(\lambda R) + \frac{-B_1\eta_2\eta_t + B_t\eta_1\eta_2}{A\eta_t^2}h(\lambda R) - \frac{B_0 B_t}{\eta_t}$$
$$\langle u_2\rangle = u_{s,2} - \frac{\eta_1}{\eta_t}(u_{s,2}-u_{s,1})h(\lambda R) + \frac{-B_2\eta_1\eta_t + B_t\eta_1\eta_2}{A\eta_t^2}h(\lambda R) - \frac{B_0 B_t}{\eta_t} \quad (36)$$

in which now B_α stands for:

$$B_\alpha = \frac{dP_\alpha}{dx}, \qquad B_t = \frac{dP_t}{dx} \quad (37)$$

Analogously to the single component description of Maxwell [23] we now put for the slip velocities

$$u_{s,\alpha} = -G_\alpha \frac{du_\alpha}{dr} \quad (38)$$

in which G_α is the slip modulus (Gleitmodulus):

$$G_\alpha = \frac{1}{2}\eta_\alpha(2\pi)^{1/2}(P_\alpha\rho_\alpha)^{-1/2}\left(\frac{2}{f_r}-1\right) \quad (39)$$

with f_r the coefficient of reflection.

Also it can be derived,

$$G_\alpha = \frac{2\eta_\alpha D_\alpha^K}{P_\alpha R} \quad (40)$$

in which D_α^K is the effective Knudsen diffusion coefficient of α, which can be approximated by [4]:

$$D_\alpha^K \approx 0.89 D_\alpha^{K0}, \quad D_\alpha^{K0} = \frac{2}{3}R\left(\frac{8R_gT}{\pi M_\alpha}\right)^{1/2} \quad (41)$$

After a lengthy derivation we find the following expressions for the *slip velocities*, in which for convenience we have expressed the pressure gradients as B_1 and B_2:

$$u_{s,1} = -\frac{1}{F}(K_{11}B_1 + K_{12}B_2),$$
$$u_{s,2} = -\frac{1}{F}(K_{21}B_1 + K_{22}B_2) \quad (42)$$

with

$$K_{11} = \frac{D_1^K}{P_1}\left[\frac{\eta_1}{\eta_t}h + (1-h)\right] + \frac{D_1^K D_2^K(1-h)}{P_t\mathcal{D}_{12}},$$
$$K_{12} = \frac{D_1^K}{P_1}h + \frac{D_1^K D_2^K(1-h)}{P_t\mathcal{D}_{12}}$$
$$K_{21} = \frac{D_2^K}{P_2}h + \frac{D_1^K D_2^K(1-h)}{P_t\mathcal{D}_{12}},$$
$$K_{22} = \frac{D_2^K}{P_2}\left[\frac{\eta_2}{\eta_t}h + (1-h)\right] + \frac{D_1^K D_2^K(1-h)}{P_t\mathcal{D}_{12}} \quad (43)$$

We will use also the following notations:

$$\zeta_\alpha = \frac{D_\alpha^K}{\mathcal{D}_{\alpha\beta}}, \quad D_{\alpha\beta}^K = x_\beta D_\alpha^K + x_\alpha D_\beta^K, \quad \zeta_{\alpha\beta} = \frac{D_{\alpha\beta}^K}{\mathcal{D}_{\alpha\beta}} \quad (44)$$

and F in Eq. (42) is given as

$$F = 1 + (1-h)\zeta_{12} \quad (45)$$

From this we can also express the cross-section averaged velocities:

$$\langle u_1\rangle = -\frac{1}{F}(Q_{11}B_1 + Q_{12}B_2),$$
$$\langle u_2\rangle = -\frac{1}{F}(Q_{21}B_1 + Q_{22}B_2) \quad (46)$$

$$Q_{12} = Q_{21} = \mathcal{D}_{12}\left\{\frac{1}{P_t}\zeta_1\zeta_2(1-h) + \frac{h}{P_t x_1 x_2}\left[x_2\zeta_1\left(\frac{\eta_1}{\eta_t}\right)^2 + x_1\zeta_2\left(\frac{\eta_2}{\eta_t}\right)^2\right]\right\} + \frac{B_0}{\eta_t}[1 - h\varphi + (1-h)\zeta_{12}]$$
$$Q_{11} = Q_{12} + h\varphi\frac{B_0}{\eta_1} + \frac{D_1^K}{P_1}(1-h),$$
$$Q_{22} = Q_{12} + h\varphi\frac{B_0}{\eta_2} + \frac{D_2^K}{P_2}(1-h) \quad (47)$$

4. Exploration of the model equations: average velocities

In all of the following the capillary geometry has been considered.

4.1. Comparison with the binary friction model: liquids

The equations for the binary friction model for liquids can be written as [4]:

$$c_\alpha\left.\frac{d\mu_\alpha}{dx}\right|_T = -c_t R_g T\sum_\beta \Phi_{\alpha\beta}\frac{x_\alpha x_\beta}{\mathcal{D}_{\alpha\beta}}(\langle u_\alpha\rangle - \langle u_\beta\rangle) - c_t R_g T(\beta_{\alpha m})^{BFM}\langle u_\alpha\rangle \quad (48)$$

in which $\Phi_{\alpha\beta}$ was introduced to account for deviations of the diffusion coefficients inside the pores from those in infinite fluids. We found that for ultrafiltration of aqueous solutions of large molecules like PEG-3400 and dextran T70 in good approximation we could work with $\Phi_{\alpha\beta} = 1$ [3,5]. The component-wall friction coefficients in the BFM are

$$(\beta_{\alpha m})^{BFM} = \frac{\phi_\alpha\kappa_\alpha}{B_0} = \frac{c_\alpha\bar{V}_\alpha\kappa_\alpha}{B_0} \quad (49)$$

and the fractional viscosity coefficients κ are related to the partial viscosities by

$$\kappa_\alpha = \frac{\eta_\alpha}{c_t R_g T\phi_\alpha} \quad (50)$$

In Fig. 3 the fractional viscosity coefficients are compared to that of water for PEG-3400 and dextran T70.

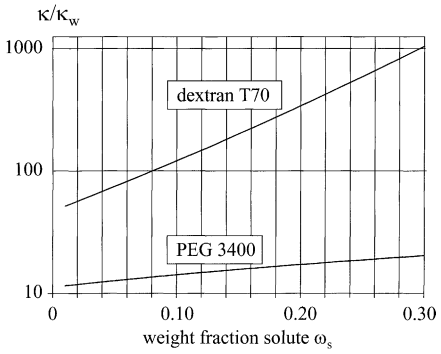

Fig. 3. Fractional viscosity coefficients of PEG-3400 and dextran T70, in relation to the weight fraction of solute, compared to those of water. Data obtained from free-liquid viscosity data [4,5,25].

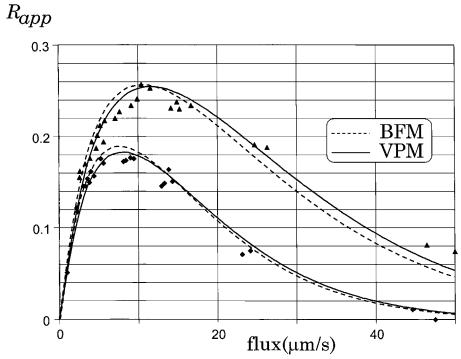

Fig. 5. Apparent rejection of PEG-3400 during ultrafiltration of aqueous solutions in a tubular module, in dependence of the flux, for two liquid circulation velocities. Drawn line: VPM-1, dotted line: BFM.

By elimination of B_t from Eq. (30) we obtain an equation which is similar to the BFM equation

$$c_1 \frac{d\mu_1}{dx}\bigg|_T = -c_t R_g T g_D \frac{x_1 x_2}{\mathcal{D}_{12}}(\langle u_1\rangle - \langle u_2\rangle) - c_t R_g T (\beta_{1m})^{VPM}\langle u_1\rangle \quad (51)$$

and an analogous one for component 2. With respect to the Lightfoot- or BFM-approximation we see here that the averaging of the velocities over the pore introduces a *diffusion averaging factor* g_D into the Maxwell–Stefan term. For liquids this factor is found to be:

$$g_D = \frac{1}{h} - \varphi \quad (52)$$

and for the wall friction factors we find

$$(\beta_{\alpha m})^{VPM} = \frac{\eta_\alpha}{c_t R T B_0} = (\beta_{\alpha m})^{BFM} \quad (53)$$

In Fig. 4, we have plotted the values of the diffusion averaging factor for both geometries, with limit values equal to 1.2 for the plates and $\frac{4}{3}$ for the capillary. It is clear that for low values of the modulus φ there is only a small deviation of this factor from unity, and so there the results of the BFM are

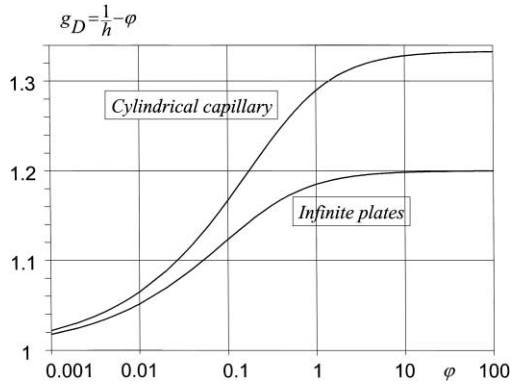

Fig. 4. The correction function g_D for use in the pore-averaged Maxwell–Stefan equations, for liquids.

in good agreement with those of the new model. At higher values of φ we will have a maximum deviation of 33% in the diffusion term for a capillary; however, increasing φ also means a higher contribution of the wall friction term, and so the deviations in the total force will be less. In Fig. 5 we show the apparent rejection of PEG-3400 in a tubular membrane module in dependence of the flux, comparing the results of the new VPM with those of the earlier BFM, for two circulation velocities. All relevant physical data, as well as the description of the boundary layer model for the flowing feed liquid, can be found in [4,24–26]. We see that there is only a slight difference between the results of the two models.

4.2. Comparison with the binary friction model: gases

For gases the BFM equations read as follows:

$$\frac{dP_\alpha}{dx} = -\sum_\beta \Phi_{\alpha\beta}\frac{P_t x_\alpha x_\beta}{\mathcal{D}_{\alpha\beta}}(\langle u_\alpha\rangle - \langle u_\beta\rangle) - (f_{\alpha m})^{BFM}\langle u_\alpha\rangle P_\alpha \quad (54)$$

and again in comparing theory with experimental data we found that $\Phi_{\alpha\beta} = 1$ did lead to good results. For the friction factor we developed the expression:

$$(f_{\alpha m})^{BFM} = \left(D_\alpha^K + \frac{B_0}{\kappa_\alpha}\right)^{-1} \quad (55)$$

and for gases we find from the Wilke relationship [27]:

$$\kappa_\alpha = \frac{\eta_\alpha}{x_\alpha P_t} = \frac{1}{P_t}\frac{\eta_\alpha^0}{\sum_\beta x_\beta \xi_{\alpha\beta}} \quad (56)$$

with η_α^0 the pure-component viscosity, and the Wilke parameters given by

$$\xi_{\alpha\beta} = \frac{[1 + (\eta_\alpha^0/\eta_\beta^0)^{1/2}(M_\beta/M_\alpha)^{1/4}]^2}{[8(1 + M_\alpha/M_\beta)]^{1/2}} \quad (57)$$

Again we can derive the friction-type equation from the foregoing results:

$$\frac{dP_1}{dx} = -g_D \frac{P_t x_1 x_2}{\mathcal{D}_{12}}(\langle u_1\rangle - \langle u_2\rangle) - (f_{1m})^{VPM}\langle u_1\rangle P_1,$$
$$\frac{dP_2}{dx} = -g_D \frac{P_t x_1 x_2}{\mathcal{D}_{12}}(\langle u_2\rangle - \langle u_1\rangle) - (f_{2m})^{VPM}\langle u_2\rangle P_2 \quad (58)$$

For the velocity averaging factor we find

$$g_D = \frac{[1 + (1-h)\zeta_{12}]Q_{12}}{d_1 d_2 + (d_1 + d_2)Q_{12}} \quad (59)$$

with

$$d_1 = h\frac{\eta_2}{\eta_t} + (1-h)x_2\zeta_1, \qquad d_2 = h\frac{\eta_1}{\eta_t} + (1-h)x_1\zeta_2 \quad (60)$$

and for the wall friction factors:

$$(f_{1m})^{VPM} = \frac{x_2}{\mathcal{D}_{12}} d_2 \frac{1 + (1-h)\zeta_{12}}{d_1 d_2 + (d_1 + d_2)Q_{12}},$$
$$(f_{2m})^{VPM} = \frac{x_1}{\mathcal{D}_{12}} d_1 \frac{1 + (1-h)\zeta_{12}}{d_1 d_2 + (d_1 + d_2)Q_{12}} \quad (61)$$

In Fig. 6, we compare the VPM results with the experimental data of Evans et al. [28,29] for counterdiffusion of He and Ar through porous graphite, and with the BFM-description. We see that the differences between the two models here are very small, and visually hard to detect. Simulations over all experimental data ranges showed a maximum deviation between the models of 2% and an average difference smaller than 0.2%. In a larger number of simulations for different gases at different pressures and pore diameters, we consistently found that the value of the averaging factor g_D was virtually equal to 1, except for a few percent deviation within the transition region. A typical example is shown in Fig. 7, for the counterdiffusion of He and Ar, where the maximum deviation from unity is about 3.5%. Numerically also the wall friction factors are very close to those of the BFM over a large region. Typically for larger pores the difference increases. In Fig. 8, again for the mentioned gases, the relative difference in friction factor is shown, and it is also seen that here the difference between the VPM and the BFM values is within a few percent. In Fig. 9 the relative difference between the predictions of the average velocities of the components by the two models is shown, and again the differences are very small. This was found again in a larger number of simulations, with one no-

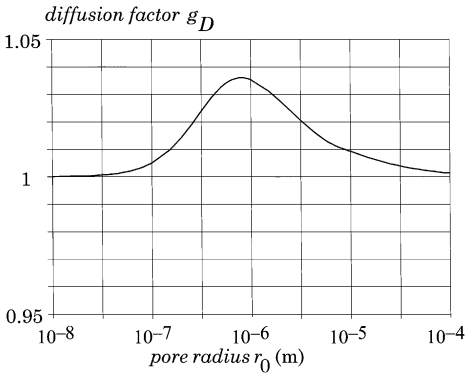

Fig. 7. Illustration of the correction function g_D for use in the pore-averaged Maxwell–Stefan equations, for the case of non-isobaric counterdiffusion of He and Ar. Purity of both gases 99%, pressure at Ar-side 2 bar, at He-side 1 bar, pore length 10^{-3} m.

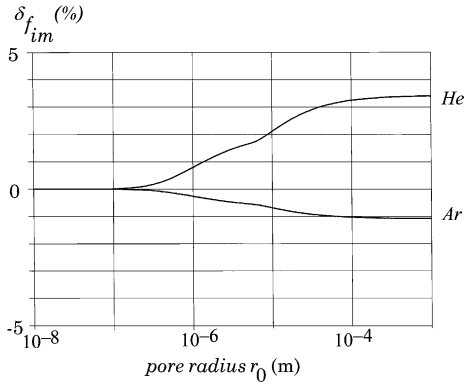

Fig. 8. Differences in component-wall friction factors as a function of pore radius, as predicted by the VPM-1 and the BFM. Isobaric diffusion at 1 bar, pore length 10^{-3} m.

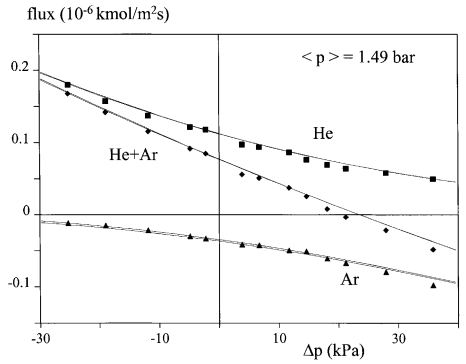

Fig. 6. Comparison of predictions of the fluxes of He and Ar through low-permeability graphite with experimental data of Evans et al. [28,29]. The predictions by the BFM and the VPM-1 are nearly indistinguishable.

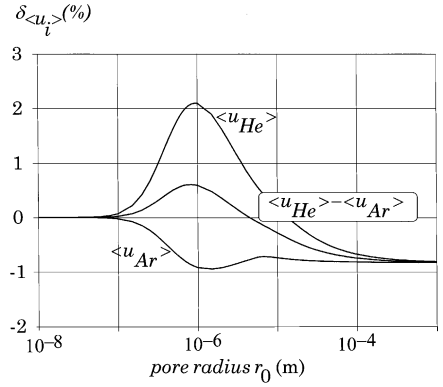

Fig. 9. Differences in predicted pore-averaged velocities between the VPM-1 and the BFM, depending on pore radius. Isobaric diffusion at 1 bar, pore length 10^{-3} m.

table exception: the isobaric counterdiffusion of components with (near-)equal mass. This will be separately discussed under Section 4.4.

4.3. The difference in average velocities

In their approach through statistical mechanics Zhdanov and Roldughin derived for a capillary, relations for the so-called diffusion velocity; in view of the large confusion of terminology as discussed elsewhere [4], we prefer here to indicate this as the difference in average velocity. They provide three expressions, one for the Knudsen region, one for the normal region and one for the transition region. Their results may be written as

$$\langle u_1\rangle - \langle u_2\rangle = -\frac{1}{x_1x_2}[\mathcal{D}_{12}]_1(\nabla x_1 + [\alpha_p]_1 x_1x_2\nabla\ln P_t + [\alpha_T]_1 x_1x_2\nabla\ln T) \quad (62)$$

which for isothermal transport goes over in

$$\langle u_1\rangle - \langle u_2\rangle = -\frac{1}{x_1x_2}[\mathcal{D}_{12}]_1(\nabla x_1 + [\alpha_p]_1 x_1x_2\nabla\ln P_t) \quad (63)$$

For the different regions they have

$$\text{Knudsen}: \quad \alpha_p = \alpha_p^K = \frac{D_1^K - D_2^K}{\mathcal{D}_{12}} = \zeta_1 - \zeta_2,$$

$$\text{normal}: \quad \alpha_p = \alpha_p^v = \frac{1}{\eta_t}\left(\frac{\eta_2}{x_2} - \frac{\eta_1}{x_1}\right),$$

$$\text{transition}: \quad \alpha_p = \frac{1}{2}(\alpha_p^K + \alpha_p^v) \quad (64)$$

From the VPM-1 model it follows:

$$\langle u_1\rangle - \langle u_2\rangle = -\frac{(1-h)(D_{12}^K/x_1x_2)[\nabla x_1 + x_1x_2\beta_p^K\nabla\ln P_t] + h(\mathcal{D}_{12}/x_1x_2)[\nabla x_1 + x_1x_2\beta_p^v\nabla\ln P_t]}{1 + (1-h)(D_{12}^K/\mathcal{D}_{12})} \quad (65)$$

with

$$\beta_p^K = \frac{D_1^K - D_2^K}{D_{12}^K}, \qquad \beta_p^v = \frac{x_1\eta_2 - x_2\eta_1}{\eta_t} \quad (66)$$

For low values of the modulus φ the value of the function h approaches unity, and so we are in the normal region. In that case only the second term on the r.h.s. of Eq. (65) remains, the denominator goes to 1, and the result is equal to that of the ZR-equation. For very high values of φ, the function h tends to $1/\varphi$, and so only the first term in the r.h.s. of (65) is important. Also for high φ, which can be encountered, e.g., for very small pores and/or very low pressures, the ratio $D_{12}^K/\mathcal{D}_{12}$ tends to zero, and so we have again the same limit as the ZR-equations. For intermediate values the present Eq. (65) provides a smooth transition between the two regions, while the ZR-equation more likely represents a single-point approximation. It should be noted

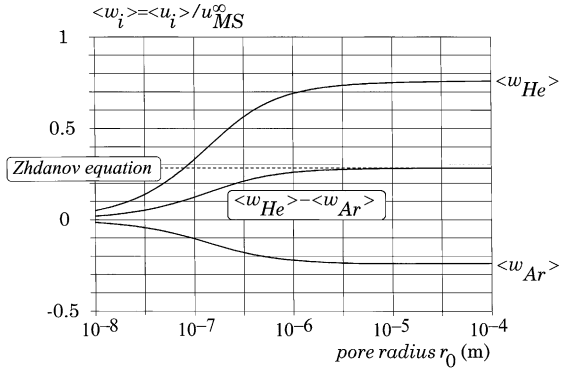

Fig. 10. Predicted pore-averaged velocities, for isobaric counterdiffusion of He and Ar. Purity of each component 99%, total pressure 1 bar. Also shown is the difference in the average velocities as predicted by Eq. (65), compared to the results of Zhdanov and Roldughin, Eq. (62), pore length 10^{-3} m.

that the authors point out that their transition equation holds only for small Knudsen layers [20]. Although much of the mathematics used in the statistical-mechanics approach is hardly tractable for the average chemical engineer, it is very clear that at several points in the derivations, approximations are made by limited series development in terms of Sonine polynomials, and discarding higher-order terms. In the ZR-papers a considerable focus was on the thermodiffusion effect, and so in that respect they applied higher-order expansions. That their equations are not complete can be seen for the case of isobaric diffusion, which leads to

$$\langle u_1\rangle - \langle u_2\rangle = -\frac{1}{x_1x_2}[\mathcal{D}_{12}]_1\frac{dx_1}{dx} \quad (67)$$

and so even in the Knudsen region the velocity difference would be equal to that in the normal region. This is illustrated in Fig. 10 for the isobaric counterdiffusion of He and Ar. The VPM predicts a continuous transition between the Knudsen and the normal region, while the ZR-equation only shows a constant value. Thus it is quite possible that further development in statistical mechanics will deliver a more extended model, and it will be exiting to compare this with the VPM model.

4.4. Isobaric diffusion of components with (near-)equal mass

In "two-bulb experiments" Waldmann and Schmitt [14] showed that when two reservoirs, each initially filled with a pure gas at the same pressure, are connected by a capillary, one of the gases will move faster through the tube than the other, causing an overpressure in one of the reservoirs. They showed that this also holds for gases with equal mass such as N_2–C_2H_4, and near-equal mass, such as Ar–CO_2. They also showed that at low average pressures the overpressure is at the CO_2-side, while at higher pressures this is reversed. An indication of the possible occurrence is found

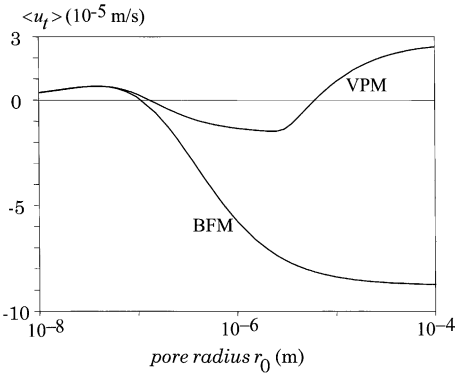

Fig. 11. Pore-averaged total velocity for isobaric counterdiffusion of Ar and CO_2 at 1 bar, as predicted by the VPM-1 and the BFM. Positive direction from Ar to CO_2, pore length 10^{-3} m.

by calculating the steady-state total pore-averaged flux at given total pressure and fixed reservoir mole fractions. We carried out such calculations for a range of pore diameters, and obtained the results as shown in Fig. 11. It is interesting that the binary friction model shows this flow reversal, as it did for the pressure effect, but that the present model predicts a second reversal point. It will be very interesting to investigate this experimentally. Also not reported to our knowledge is the effect of temperature on such phenomena. For a total pressure of 1 bar, and a tube diameter of 1 μm we calculated that there would be a flow reversal also with temperature. As can be seen in Fig. 12, there is large difference in reversal temperature between the binary friction model and the velocity profile model. Inspection of the numerical results showed that over the range investigated the differences stem from the difference between the models in the wall friction factors, which grows from 0.3% at a pore diameter of 10^{-7} m to about 10% at 10^{-4} m. Here we see that the difference between the two models is the largest, because the phenomenon of isobaric counterdiffusion with (near-)equal mass is only a very subtle one. For non-equal mass isobaric counterdiffusion and for non-isobaric diffusion the results of both the models are very close together.

5. Velocity profiles

Also here our treatment is only exploratory, since the new model offers very extended possibilities for investigation.

5.1. Liquid ultrafiltration, related to earlier experiments

The first case we considered is the ultrafiltration of aqueous PEG-3400 and dextran T-70 solutions, for which we earlier showed that the cross-section averaged models gave a good correspondence with experimental data. First we calculated the velocity profiles for the conditions corresponding to our experiments. From the integral calculations we found the difference in concentration but also in chemical potential of the components over the pore length. We evaluated the velocity profiles at the average concentration in the pore, and at the linearized gradient values of the chemical potential and total pressure. In Fig. 13 we present the pore velocity profiles of PEG-3400 and water for three values of the flux, for the WFBX-0121-membrane, at a module circulation velocity of 1.95 m s^{-1}. As a reference value we have chosen here the average velocity according to the Poiseuille equation. We see that the water velocity profile in all cases is very close to the Poiseuille profile. For a very low total flux, 10^{-6} m s^{-1}, we find that the PEG has a higher velocity than the water. With increasing flux we find that the relative velocity decreases and eventually becomes smaller than that of water. The reason for this can be found in the change in the chemical potential gradient for PEG. For the average velocity of component 1 relative to the average Poiseuille velocity we can write:

$$\frac{\langle u_1 \rangle}{\langle u_{\text{Pois}} \rangle} = 1 + \varphi h \left(\frac{B_1}{B_t} \frac{\eta_t}{\eta_1} - 1 \right) \tag{68}$$

In order to increase the flux, the external transmembrane pressure is increased; although an increased concentration polarization at the membrane surface occurs, a still higher pressure gradient inside the membrane pore results, going from -8.5×10^9 N m^{-3} through -8.4×10^{10} N m^{-3} to

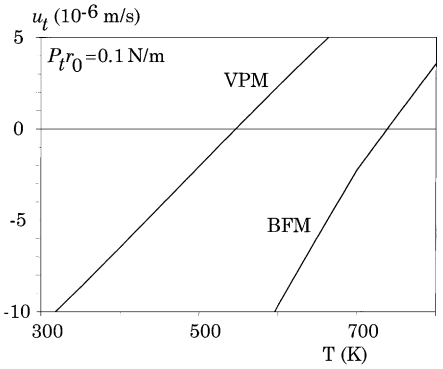

Fig. 12. Reversal prediction of the pore-averaged total velocity in dependence of temperature, for isobaric counterdiffusion of He and Ar, pore length 10^{-3} m.

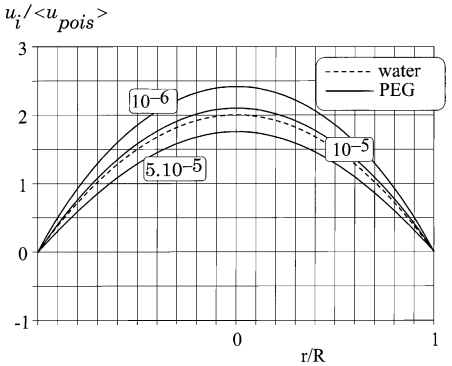

Fig. 13. Velocity profiles inside the pores during ultrafiltration of PEG-3400, as follows from the VPM-1, for three values of the transmembrane flux. Conditions as in Fig. 5.

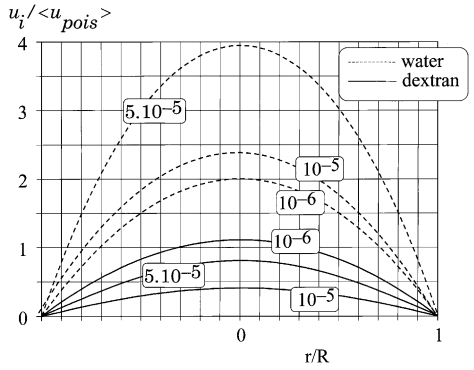

Fig. 14. Velocity profiles inside the pores during ultrafiltration of dextran T70 on YM-30 membrane in a stirred cell, as follows from the VPM-1, for three values of the transmembrane flux. Conditions described in [5,25].

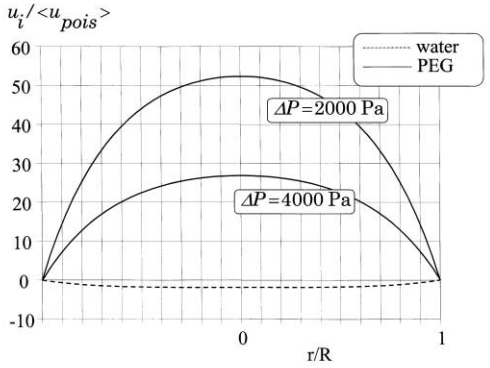

Fig. 15. Velocity profiles inside the pores during ultrafiltration of PEG-3400 on YM-30 membrane in a stirred cell, as follows from the VPM-1, for low transmembrane pressures. Parameter transmembrane pressure. Conditions described in [5,25].

$-4.3 \times 10^{11}\,\mathrm{N\,m^{-3}}$. The part taken up by the PEG in terms of its gradient B_1 goes from 10.6% through 7.3 to 4.9%, thus increasing the relative force on the water. Due to the increase in the PEG-concentration the ratio η_t/η_1 decreases, leading to a decrease in $(B_1/B_t)(\eta_t/\eta_1)$ from 1.76 through 1.19 to 0.51. The value of φh remains nearly constant, going from 0.34 to 0.3, and so we see that the relative velocity of the PEG decreases, as reflected in the velocity profiles.

In a similar simulation we took the values encountered in the UF of dextran T70 as we studied in a stirred cell with a YM30 membrane. The results of the velocity profiles are shown in Fig. 14. With increasing flux we see now that the water velocity profile becomes much more pronounced, going considerably faster than the Poiseuille profile. The behavior with increasing flux of the dextran relative velocity profile is more complex. First the dextran relatively slows down, and then the velocity increases again. Contrary to the PEG-case here the fraction of the total pressure gradient taken up by B_1 increases with increasing flux, due to a much stronger concentration polarization in the boundary layer: from 0.9% through 1.9 to 6.2%.

We find that $(B_1/B_t)(\eta_t/\eta_1)$ decreases stronger than for PEG-3400, going from 0.53 through 0.11 to 0.10. Here with increasing flux the value of φh goes down from 0.94 through 0.91 to 0.70. This causes first a decrease in relative velocity due to the strong decrease in $(B_1/B_t)(\eta_t/\eta_1)$, but at the higher flux the relative velocity increases again due to the decrease in φh.

5.2. Liquid ultrafiltration, constant concentration gradient, varying transmembrane pressure

In another set of simulations we kept the concentration gradient constant, and varied the total pressure gradient. For PEG-3400 in a YM30 membrane we calculated the velocity profiles at a concentration range over the pore from 15 to $1\,\mathrm{kg\,m^{-3}}$. In Fig. 15 the profiles are shown for PEG, again relative to the average Poiseuille velocity. It is clear that here the PEG-velocity is much larger than the Poiseuille flow. For a transmembrane pressure of 2000 Pa the gradient in chemical potential is 5.73 times the total pressure gradient, for 4000 Pa it is 2.87, and so the driving force for PEG motion is relatively lower at the higher pressure. In Fig. 16 for the same conditions an expanded view is shown for the water velocity profile. At 2000 Pa we see that the water flows against the pressure gradient. This is caused by the positive gradient in the chemical potential of water, which in this case is −4.7 times the total pressure gradient. This negative flow is thus comparable to the osmotic flow in isobaric diffusion. For 4000 Pa we see an interesting phenomenon: in the center the water moves in the positive x-direction, while for larger r-values it flows in the other direction. In the center the PEG-velocity is highest, and so the friction force with the water overcomes the water chemical potential gradient, while nearer to the wall the PEG-velocity is lower and so the water can flow backwards.

A similar simulation for dextran T70 in the same membrane for a transmembrane pressure of 200 Pa shows that

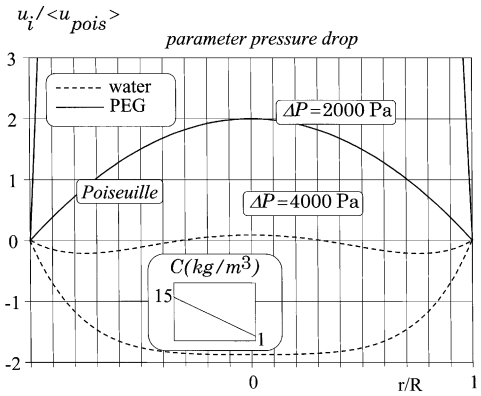

Fig. 16. Enlarged velocity profiles inside the pores during ultrafiltration of PEG-3400 on YM-30 membrane in a stirred cell, as follows from the VPM-1, for low transmembrane pressures. Conditions described in [5,25].

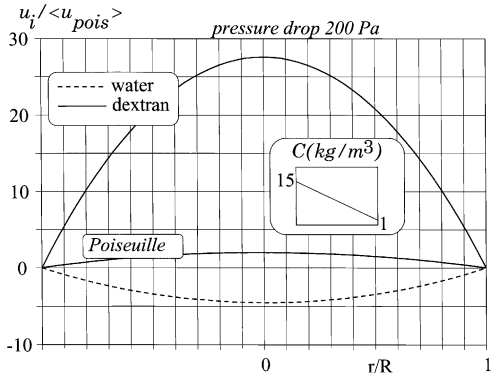

Fig. 17. Enlarged velocity profiles inside the pores during ultrafiltration of dextran T70 on YM-30 membrane in a stirred cell, as follows from the VPM-1, for low transmembrane pressures. Conditions described in [5,25].

here also the water velocity occurs against the total pressure gradient as shown in Fig. 17.

Conditions such as used here in the simulations can be attained experimentally, and so the phenomena shown here can be verified, also quantitatively. Moreover, the backward motion of water can in principle be measured by labeling with deuterium or tritium.

5.3. Isobaric and isovolumetric liquid diffusion

Here we simulated the diffusion of PEG-3400 and water in pores of different sizes, at various concentration levels. The results are shown in Fig. 18. Here we have taken as reference velocity the average velocity of PEG-3400 (component 1) in case of a very large pore size:

$$\langle u_1^{\infty} \rangle = -\frac{\eta_2}{\eta_t} \frac{\mathcal{D}_{12}}{c_t R_g T x_1 x_2} B_1 \tag{69}$$

For a low average concentration, $0.06\,\mathrm{kg\,m^{-3}}$, we see in Fig. 18a that for a pore size of 10 nm we have a strongly curved velocity profile for PEG, and the wall friction clearly slows down the diffusion. For a pore size of 100 nm we obtain over the largest part of the pore diameter a virtually flat velocity profile, with only a small region near the wall in which the velocity gradient is located. This approaches then the classical assumption of a uniform velocity profile. The region near the wall over which the velocity gradient is present becomes smaller with increasing pore size. The water velocity is very small. For a high average concentration, $60\,\mathrm{kg\,m^{-3}}$, we see in Fig. 18b again for the pore size of 10 nm a strongly curved velocity profile, and for 100 nm a flattening out. However, here we see that the water velocity is much higher. For the case of very large pores we have for the ratio of the average velocities:

$$\frac{\langle u_2^{\infty} \rangle}{\langle u_1^{\infty} \rangle} = -\frac{\eta_1}{\eta_2} = -\frac{c_1 \bar{V}_1 \kappa_1}{c_2 \bar{V}_2 \kappa_2} \tag{70}$$

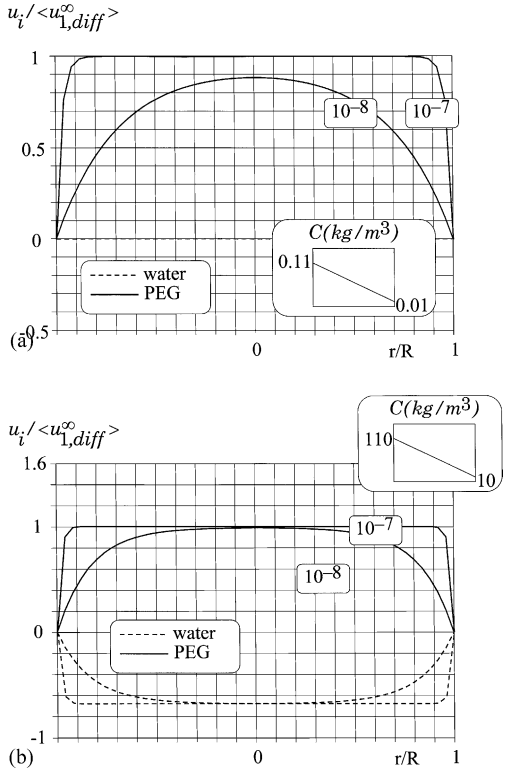

Fig. 18. (a) Velocity profiles in a pore in isobaric diffusion of PEG-3400 in aqueous solution, for very low PEG-concentration, with pore diameter as parameter. (b) Velocity profiles in a pore in isobaric diffusion of PEG-3400 in aqueous solution, for high PEG-concentration, with pore diameter as parameter.

The value of κ_1/κ_2 is only slightly dependent on concentration [4], and so with increasing value of the concentration of component 1 the velocity of component 2 increases.

It should be noted that the present model fixes the velocities and thus the fluxes for isobaric transport by means of the boundary conditions, and so even for very large pores the viscosities remain present in the expressions. The classical way to fix the fluxes for large-pore molecular diffusion is to assume isovolumetric transport. For the gradient in the total pressure we have by addition of the equations for components 1 and 2:

$$\frac{\mathrm{d}P_t}{\mathrm{d}x} = -c_t R_g T (\beta_{1m} \langle u_1 \rangle + \beta_{2m} \langle u_2 \rangle) \tag{71}$$

For isovolumetric transport we have

$$\langle u_1 \rangle c_1 \bar{V}_1 + \langle u_2 \rangle c_2 \bar{V}_2 = 0 \tag{72}$$

Combining (71), (72), (49) and (51) we obtain

$$\frac{\mathrm{d}P_t}{\mathrm{d}x} = \frac{\mathcal{D}_{12}}{B_0} c_t^2 \bar{V}_1 \bar{V}_2 (\kappa_1 - \kappa_2) c_1 \frac{\mathrm{d}\mu_1}{\mathrm{d}x} \tag{73}$$

and so, although there is a fundamental difference between isobaric and isovolumetric diffusion, at increasing pore size we see that because of the increase in B_0 the total pressure gradient for the latter situation will become very small.

From Eq. (72) it follows:

$$\left.\frac{\langle u_2\rangle}{\langle u_1\rangle}\right|_{\text{isovolumetric}} = \frac{c_1\bar{V}_1}{c_2\bar{V}_2} \tag{74}$$

and we may write for isovolumetric transport of component 1:

$$c_t R_g T\left(g_D\frac{x_1x_2}{\mathcal{D}_{12}}\frac{\eta_t}{\eta_2} - \frac{\kappa_1\phi_1}{B_0}\right)\langle u_1\rangle = B_1 \tag{75}$$

while we have for isobaric transport:

$$c_t R_g T\left(g_D\frac{x_1x_2}{\mathcal{D}_{12}}\frac{1}{\phi_2} - \frac{\kappa_1\phi_1}{B_0}\right)\langle u_1\rangle = B_1 \tag{76}$$

For large pores the second term between brackets disappears, and for very dilute solutions $\phi_2 \to 1$, and $\eta_t \to \eta_2$, and so the predictions for both situations approach each other.

An example of the other extreme may be the adsorption of large biopolymers in pellets with small pores. For such polymers we will have a large specific volume and a high value of κ, leading to a considerable gradient in total pressure, with the lowest pressure inside the pellet.

5.4. Non-isobaric counterdiffusion of gases

In Fig. 19 the velocity profiles of He and Ar are presented for the case that we have an overpressure at the Ar-side of 1 bar, and 99% purity of both gases, for several pore diameters. The parameters are evaluated at the point values halfway the capillary. For a pore diameter of 0.1 mm we see that the velocity profiles of both gases very closely approach the Poiseuille profile. For a diameter of 1 μm we see for both gases a considerable slip velocity at the wall, and a difference in velocity between Ar and He. The helium velocity is lower, because of the driving force against the direction of the Ar-flow. For 0.5 μm diameter we see an increase in slip velocity for Ar, and for He we see that the inner core is still moving in the direction of Ar-flow, but near the pore wall it is moving in the other direction, from high to low He pressure. Similar to the liquid diffusion depicted in Fig. 16, here also in the pore center the friction with the fast moving

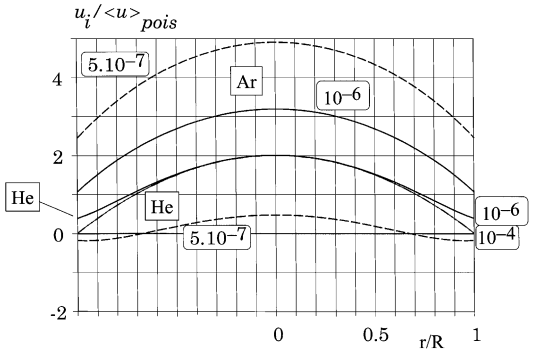

Fig. 19. Velocity profiles inside pores during non-isobaric counterdiffusion of He and Ar. Same conditions as in Fig. 7.

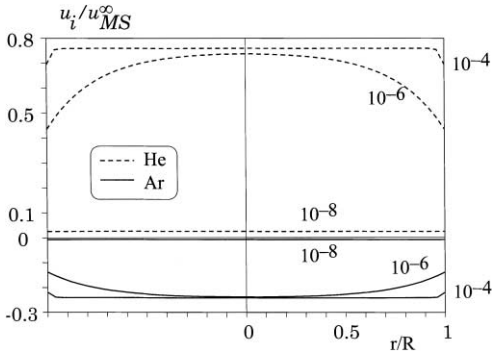

Fig. 20. Velocity profiles inside pores during isobaric counterdiffusion of He and Ar.

Ar molecules causes the He to move with them, while near the wall the friction force between the molecules is lower.

5.5. Isobaric gas diffusion

In Fig. 20 we present the velocity profiles again for He–Ar diffusion at a total pressure of 1 bar. Again we have taken the parameter and gradient values halfway the pore. Here we have normalized on the velocity difference according to an infinite medium:

$$u^{\infty}_{MS} = -\frac{\mathcal{D}_{12}}{P_t x_1 x_2}\frac{dP_1}{dx} \tag{77}$$

For a pore of 10 nm we see a virtually flat velocity profile, corresponding to Knudsen diffusion. For 1 μm we clearly have a curved velocity profile, and for 0.1 mm we have nearly flat profiles, with a small gradient to a high slip velocity at the wall. For isobaric transport we have

$$\langle u_2\rangle = -\langle u_1\rangle\frac{f_{1m}P_1}{f_{2m}P_2} \tag{78}$$

For the large pore we find $\varphi = 4.11\times10^{-5}$, and $h = 0.97$. From Eqs. (60) and (61) for $x_1 = x_2 = 0.5$ we find that for this large pore size

$$\frac{f_{1m}}{f_{2m}} \approx \frac{D_2^K}{D_1^K} = 0.316$$

Contrary to the analysis from the binary friction model we see here that both for very small and very large pores, at equal mole fractions, the velocity and so the flux ratio closely follows Graham's law; only at intermediate values of the modulus φ we have deviations.

5.6. Stefan diffusion

Here we consider the Stefan diffusion of water vapor through N_2. We assume that $\langle u_2\rangle = 0$, and so we obtain for the pressure gradient of water vapor

$$\frac{dP_1}{dx} = -g_D\frac{P_t x_1 x_2}{\mathcal{D}_{12}}\langle u_1\rangle - f_{1m}\langle u_1\rangle P_1 \tag{79}$$

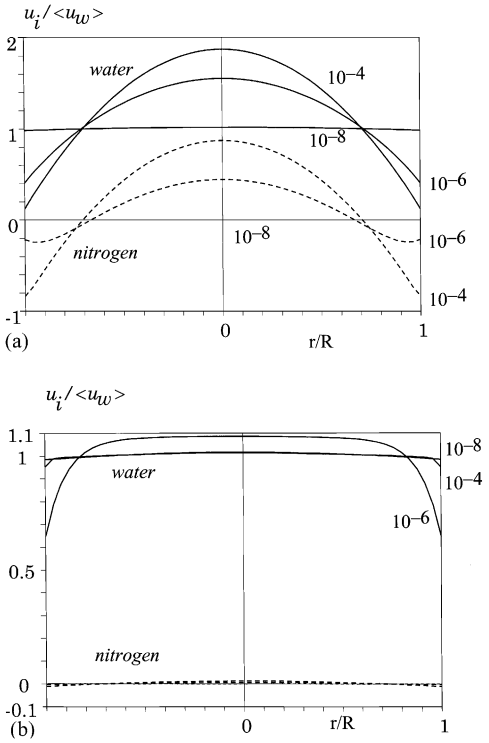

Fig. 21. Velocity profiles of water and nitrogen in a Stefan-tube at: (a) high mole fraction of water; (b) low mole fraction of water; pore-average velocity of nitrogen is equal to zero. Pore diameter as parameter, pore length 10^{-3} m.

from which follows:

$$\langle u_1 \rangle = -\frac{1}{g_D(P_t x_1 x_2/\mathcal{D}_{12}) + f_{1m} P_1} \frac{dP_1}{dx},$$
$$\frac{dP_2}{dx} = -\frac{g_D(P_t x_1 x_2/\mathcal{D}_{12})}{g_D(P_t x_1 x_2/\mathcal{D}_{12}) + f_{1m} P_1} \frac{dP_1}{dx} \quad (80)$$

Here we choose a value of (dP_1/dx) and of P_1, and by this choice the other parameters follow, including the gradient in total pressure. In Fig. 21a, we present the velocity profiles for water vapor and air for three pore diameters, at a high mole fraction of water. For the 10 nm pore we have again Knudsen diffusion, and the air velocity profile is flat. For a pore of 1 μm we see a strongly curved velocity profile for water, and also for nitrogen. In the center of the pore the nitrogen is dragged along by the fast water vapor, and since the total flux is zero, near the walls the nitrogen has to flow into the other direction. This is even stronger for the 0.1 mm pore. It also means that near the water surface these profiles cannot hold anymore, but that a circulation of nitrogen from the outer annulus towards the inner core has to take place. Also this may be verified by a suitable experiment, e.g. by injecting a detectable tracer in the gas stream flowing over the outlet of the Stefan-tube.

In Fig. 21b the velocity profiles are shown for a low mole fraction of water. For the 10 nm pore, as well as for the 0.1 mm pore, we see essentially nearly a flat velocity profile, with a very small gradient at the side. For a 1 μm pore we have a more curved velocity profile for the water vapor. Here we see that the velocities of the nitrogen are virtually equal to 0 over the whole pore cross-section. Thus, if we specify a large enough capillary diameter for our students test, the error made in using the very simple Stefan equation without wall effects, is very small. For modeling drying processes with pores in the 0.1–1 μm range, however, we need to be more precise.

6. Concluding remarks

We have developed here a model for a single pore, without radial transport. As such this is applicable to, e.g. membrane ultrafiltration, diaphragm diffusion cells, transport studies in capillaries, and membrane reactors with inert pore surfaces. From the comparison with experimental data it is clear that the integrated velocities represent a close approximation of the transport processes actually happening. We made plausible that in the momentum balance for a component the shear term should be incorporated, but limited to the velocity gradient of this component. Also it was made clear that there lies a challenge in the field of statistical mechanics study of this type of phenomena, since the present equations from this field are insufficient. As shown, the earlier presented binary friction model gives in many cases results which are very close to the new model, with the exception of isobaric counterdiffusion of gases of near-equal mass. Since the BFM is not limited to binary systems, it may still be considered a good working theory until further development of velocity profile model has been done.

We have demonstrated the application of the present theory in a number of examples. There is a lot more work to be done in this area. In the earlier work the transport in macro- and mesopores has generally been considered as one-dimensional. However, in heterogeneous catalysis, adsorption and drying we have radial transport to and from the pore wall. The equations presented here for the most simple transport case can be easily extended to more-dimensional transport, and can at least be solved numerically by most commercial CFD packages. This will enable the study of to what degree simplified models are sufficient to describe these more complex phenomena.

Another logical study is the development of the present theory towards multicomponent systems.

We feel that the present treatment may contribute to a more realistic understanding of pore transport, in contrast to previous work based on only estimates of pore-averaged fluxes without fundamental underpinning. In communicating these phenomena no more use is needed of mystifying terminology, such as a large variety of fluxes. In the present form the theory is accessible to undergraduate level, and as such may aid in teaching mass transfer phenomena.

Acknowledgements

The major part of this work was carried out during a sabbatical leave of one of us (PK) at the Universidade Estadual de Campinas, at the Departamento de Termofluidodinâmica of the Faculdade de Engenharia Quimica, on invitation by Prof. Maria Aparecida Silva. This stay was supported by the Fundação de Amparo à Pesquisa do Estado de São Paulo (FAPESP) No. 1999/2339-6. We thank Dr. A. Kronberg of Twente University for making available to us his unpublished results in the report of Schoorlemmer [22].

Appendix A

The equations for the VPM can also be written in terms of the fluxes through $\langle N_\alpha \rangle = \langle u_\alpha \rangle c_\alpha$. For binary liquids we obtain

$$N_1 = u_1 c_1 = -\frac{\Gamma_{c1}}{G}\frac{dc_1}{dx} + u^v \frac{F}{G} c_1, \quad F = \frac{g_D}{\mathcal{D}_{12}} + \frac{c_t^2 V_1 V_2}{B_0}\kappa_2,$$

$$G = \frac{g_D}{\mathcal{D}_{12}} + \frac{c_t}{B_0}(\phi_2\kappa_1 V_1 + \phi_1\kappa_2 V_2)$$

with

$$\Gamma_{c1} = 1 + c_1 \frac{d\ln\gamma_1}{dc_1} - \frac{c_1}{c_t}\left(1 - \frac{\bar{V}_1}{\bar{V}_2}\right)$$

References

[1] E.A. Mason, A.P. Malinauskas, R.B. Evans III, J. Chem. Phys. 46 (1967) 3199.
[2] E.A. Mason, L.A. Viehland, J. Chem. Phys. 68 (1978) 3562.
[3] P.J.A.M. Kerkhof, Chem. Eng. J. 64 (1996) 319.
[4] E.N. Lightfoot, Transport in Living Systems, Wiley, New York, 1974.
[5] P.J.A.M. Kerkhof, Latin Am. Appl. Res. 28 (1998) 15.
[6] R.J. Wijngaarden, A. Kronberg, K.R. Westerterp, Industrial Catalysis, Wiley/VCH, Weinheim, 1998.
[7] F. Keil, Diffusion und Chemische Reaktionen in der Gas/Feststoff-Katalyse, Springer, Berlin, 1999.
[8] J.A.C. Silva, A.E. Rodrigues, AIChE J. 43 (1997) 2524.
[9] P.J.A.M. Kerkhof, I&EC Res. 36 (1997) 915.
[10] S. Whitaker, Chem. Eng. Ed. 22 (1988) 104.
[11] S. Whitaker, The Development of Fluid Mechanics in Chemical Engineering, in: N. Peppas (Ed.), One Hundred Years of Chemical Engineering, Kluwer Academic Publishers, Dordrecht, 1989, p. 45.
[12] S. Whitaker, Ind. Eng. Chem. Res. 30 (1991) 978.
[13] H.A. Kramers, J. Kistemaker, Physica X 8 (1943) 699.
[14] L. Waldmann, K.H. Schmitt, Z. Naturforsch. 16A (1961) 1343.
[15] H. Lang, K. Eger, Z. Phys. Chem. Neue Folge 68 (1969) 130.
[16] H. Lang, Ber. Bunsengesellschaft 79 (1975) 758.
[17] H. Lang, S.K. Loyalka, Phys. Fluids 13 (1970) 1871.
[18] V.M. Zhdanov, V.I. Roldughin, Physica A 199 (1993) 291.
[19] V.M. Zhdanov, V.I. Roldughin, JETP 78 (1994) 170.
[20] V.M. Zhdanov, Adv. Coll. Int. Sci. 66 (1996) 1.
[21] A.E. Kronberg, Unpublished results, 1996.
[22] J.P. Schoorlemmer, Gas transport in capillaries and porous media, Ir-Thesis, Twente University, November 1996.
[23] J.C. Maxwell, in: W.D. Niven (Ed.), Scientific Papers, Vol. II, Dover, New York, 1965, p. 86, 681.
[24] C.W. van Oers, Solute rejection in multicomponent systems during ultrafiltration, Ph.D. Thesis, Eindhoven University of Technology, 1994.
[25] C.W. van Oers, M.A.G. Vorstman, P.J.A.M. Kerkhof, J. Memb. Sci. 73 (1995) 231.
[26] C.W. van Oers, M.A.G. Vorstman, R.v.d. Hout, P.J.A.M. Kerkhof, J. Memb. Sci. 136 (1997) 71–87.
[27] R.C. Reid, J.M. Prausnitz, T.K. Sherwood, The Properties of Gases and Liquids, McGraw-Hill, New York, 1977.
[28] R.B. Evans, G.M. Watson, J. Truitt, J. Appl. Phys. 33 (1962) 2682.
[29] R.B. Evans, G.M. Watson, J. Truitt, J. Appl. Phys. 34 (1963) 2020.